Korean J. Chem. Eng., 40(10), 2572-2580 (2023)
DOI: 10.1007/s11814-023-1497-9

pISSN: 0256-1115
eISSN: 1975-7220

CFD modeling of a multichannel Fischer-Tropsch reactor module with microscale cooling channels: Effects of mirrored structure cooling layers

Yesol Woo*, Da Bin Oh, Jae Eun Park**, Seung Ju Han***, Yun-Jo Lee***, and Myung-June Park*,**,†**

*Department of Energy Systems Research, Ajou University, Suwon 16499, Korea
**Department of Chemical Engineering, Ajou University, Suwon 16499, Korea
***C1 Gas & Carbon Convergent Research Center, Korea Research Institute of Chemical Technology (KRICT), Daejeon 34114, Korea

(*Received 28 March 2023 • Revised 15 May 2023 • Accepted 22 May 2023*)

Abstract−Computational fluid dynamics (CFD) modeling of a multichannel Fischer-Tropsch reactor with microscale cooling channels is addressed in this study, wherein detailed mass, momentum, and energy balances were solved to retrieve detailed distributions of the conversion and temperature of both catalytic and cooling layers. A comparison between experimental data and simulation results showed relative errors of 6.73% and 1.22% for conversion and C_{5+} selectivity, respectively, which proves the validity of the proposed model. The novel structure of the reactor composed of mirrored structure cooling layers is suggested to prevent the thermal instability of a large-scale reactor module. The simulation showed that the symmetric distribution of the dense cooling channel area in the early part of the reactor decreased peak temperatures (ΔT_{max}=28.6 °C), whereas the nonmirrored case resulted in hot spots caused by the limited heat transfer capacity (ΔT_{max}=39.2 °C). The effects of the feed/coolant temperature, space velocity, and pressure were evaluated, and high temperatures and pressures resulted in a steep temperature increase in the early part of the reactor, whereas the high space velocity showed an increase in the area of peak temperature. Further, the analysis showed trade-offs of operating conditions between the conversion and selectivity of desired products.

Keywords: Fischer-Tropsch, Multichannel Reactor, Microscale Cooling Channels, Mirrored Cooling Layer, CFD Modeling

INTRODUCTION

The catalytic conversion of syngas (mixtures of CO and H_2) to hydrocarbons is the most important process for improving carbon cycling given increasing energy demand and environmental concern [1,2]. Fischer-Tropsch synthesis (FTS), which converts syngas to liquid hydrocarbons, is a promising option for ensuring the continuation of the petrochemical industry with its dwindling oil reserves. Iron and cobalt-based catalysts are typically used in FTS; however, recent interest has focused on cobalt FTS catalysts stimulated by developments at Shell and Exxon as new and substantially economical processes for converting natural gas to high-quality middle-distillate and diesel fuels [3,4].

The kinetics of FTS on cobalt catalysts has received significant research attention. For example, Zennaro et al. [5] applied the power-law model and Langmuir-Hinshelwood (LH) type rate equations with different reaction orders and site balance equations to the experimental data over the Co/TiO_2 catalyst, and demonstrated that the LH rate fitted the best and was similar to the model proposed by Yates and Satterfield [6]. Keyvanloo et al. [7] exploited several FTS reaction mechanisms for cobalt FT catalyst and derived LH rate models based on different CO dissociation methods, rate-limiting steps, and most abundant surface intermediates. A kinetic model was developed to describe the lumped distribution of the FTS product by combining the Langmuir-Hinshelwood-Hougen-Watson (LHHW) carbide mechanistic approach and thermodynamic correlation [8]. Another approach involved combining the alkyl/alkenyl mechanism for FTS and the formate mechanism of the water-gas-shift (WGS) reaction for cobalt-based catalyst on a SiO_2 support [9]. A review of the published kinetic rate models was reported previously [10], wherein 12 of the reported models were used to investigate their behavior in six different scenarios (various H_2/CO ratios, over/under stoichiometric feed composition, and with/without added water).

The high exothermic nature of the FT reaction requires an active coolant with a high heat removal capacity and motivates research on the effective design of reactors with high heat transfer requirements. Fratalocchi et al. [11] experimentally demonstrated the adoption of a Fischer-Tropsch tubular reactor loaded with highly conductive open-cell aluminum foam packed with catalyst microspheres to enhance heat exchange. Deshmukh et al. [12] studied a pilot-scale microchannel reactor with 276 process channels and 132 coolant channels arranged in a cross-flow configuration to meet the enhanced level of heat removal. A similar reactor shape was considered in Shin et al.'s work, which showed that the cooling performance of the cross-current channel was as good as that of the counter-current case [13]. Recently, computational fluid dynamics (CFD) tools have been used to conduct simulations for the performance analysis of FTS reactors. Arzamendi et al. [14] evaluated the buoyancy effect on the thermal behavior of a microchannel reactor block, and Shin et al. [15] simulated a channel-type reactor with a

†To whom correspondence should be addressed.
E-mail: mjpark@ajou.ac.kr
Copyright by The Korean Institute of Chemical Engineers.

plate heat exchanger for cobalt-based FTS using CFD to indicate that the increased heat transfer rate in the channel-type reactor resulted in a nearly isothermal operation in the catalytic bed. The temperature was satisfactorily controlled even when the modules were increased for high capacity. Shin et al's work was further expanded for determining the optimal structure of a modular multichannel reaction module [16]. The CFD simulation of heat transfer in a microchannel reactor block for low-temperature FTS (LTFT) was used to modify the reactor block with improved thermal performance and heat transfer enhancements attributed to wall boiling conditions [17]. Recent studies for innovative configurations such as monolithic loop and membrane reactors as well as microchannel reactors for improving the performance of LTFT synthesis have been reported [18].

In the present study, a CFD simulation was applied to retrieve the detailed distributions of conversion and temperature for a more complicated description of the multichannel Fischer-Tropsch reactor with microscale cooling channels. The validity of the developed model was corroborated using experimental data from the pilot plant, and then the model was used to prove the effectiveness of the alternate stack of mirrored structure cooling layers for obviating local hot spots. The effects of operating conditions on the catalytic performance and thermal stability of the proposed structure were evaluated.

EXPERIMENTAL AND MODELING METHODS

1. Catalyst Preparation

A Pt-Co/Si-Al_2O_3 catalyst was synthesized by the wet-impregnation method to operate the Fischer-Tropsch pilot plant with a multichannel reactor. 23 wt% cobalt and 0.05 wt% platinum were impregnated on a Si-coated Al_2O_3 support (surface area 170 m^2/g. Puralox®) to yield a Pt-Co/Si-Al_2O_3 catalyst. Cobalt (II) nitrate hexahydrate and tetraamine platinum (II) nitrate were used as metal precursors for the impregnation. After multiple wet-impregnation steps, the resultant solid was calcined at 350 °C for 5 h.

2. Experimental Setup

The Fischer-Tropsch pilot plant was operated using the multichannel reactor containing 15 catalytic bed layers with 9 channels each (Fig. 1(a)). The dimensions of the reactor were 165×165×450 mm, while detailed information on the size of the catalytic bed is not provided owing to the nondisclosure agreement. The catalyst bed channels were filled with 1.73 kg of SiC (200-300 μm, bulk density: 690 kg/m^3) and 1.20 kg of the catalyst (60-150 μm, bulk density: 1,308 kg/m^3). Before the reaction, the catalysts were pre-treated under 5% H_2/Ar flow at 400 °C for 5 h. A reaction test was conducted for 80 h at a reaction temperature of 235 °C, pressure of 2.0 MPa, and space velocity of 6,600 mL/(g_{cat}·h). During the reaction, the molar ratio of H_2/CO was in the range 2.2-2.5. In the coolant flow channel of the multichannel reactor, the water flow rate was 2,000-2,200 mL/min under 2.7-3.0 MPa. Gaseous products (CO_2, CO, CH_4, and Ar) were analyzed by online gas chromatography (GC, YL instrument) with a thermal conductivity detector and columns packed with a Porapak Q/molecular sieve (5 Å). Further, C_1 to C_4 hydrocarbons were measured using a flame ionization detector with a GS-GasPro capillary column.

3. CFD Modeling

CFD modeling of the reactors was conducted using COMSOL

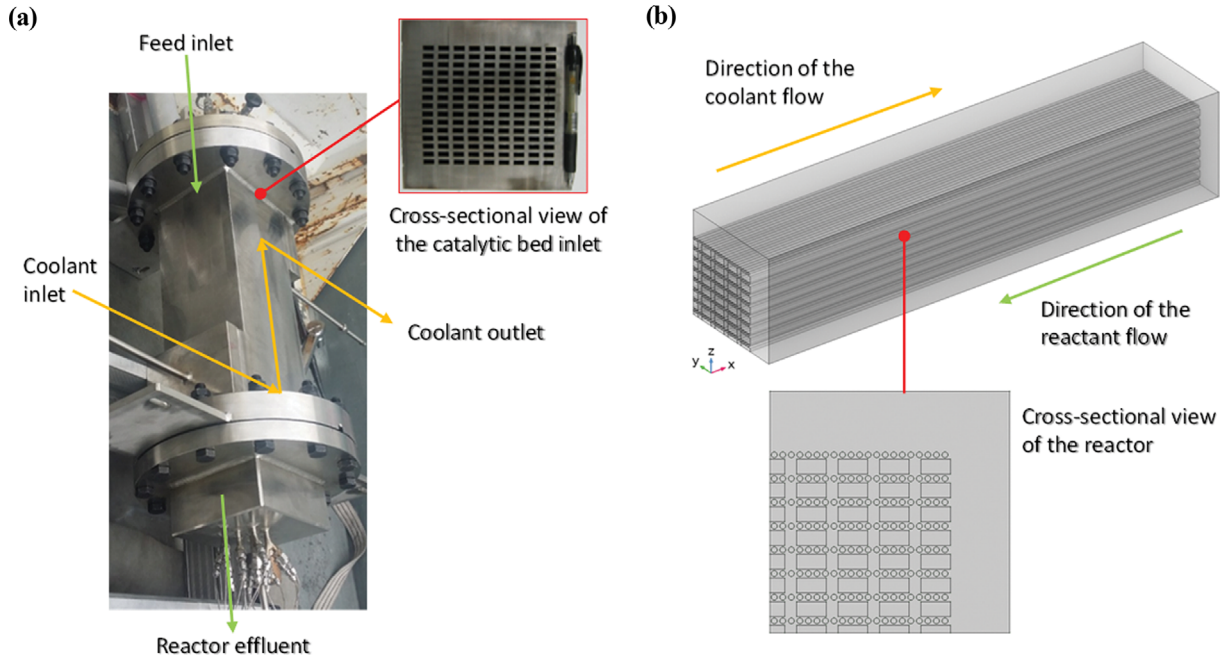


Fig. 1. (a) Actual images of the multichannel FTS reactor with microscale cooling channels for producing 0.2 barrels per day (BPD) and (b) the schematic of the multichannel FTS reactor with microscale cooling channels for CFD modeling. The symmetry condition was applied and one-fourth of the entire reactor was simulated; the number of catalytic bed layers is 15, and each layer has 9 channels for catalytic loading. The experimental conditions for pressure, SV, and temperature (both inlet and wall) are 2 MPa, 6,600 mL/(g_{cat}·h), and 225 °C, respectively. The feed composition was set as H_2/CO=2.

Table 1. Detailed stationary equations used in each part of the module

Name	Balance equations	Remarks
Transport of concentrated species	$\nabla\cdot\mathbf{j}_i+\nabla\cdot(\rho\omega_i\mathbf{u})=\mathrm{R}_i$ where $\mathbf{j}_i=-\left(\rho\mathrm{D}_i^m\nabla\omega_i+\rho\omega_i\mathrm{D}_i^m\frac{\nabla\mathrm{M}_n}{\mathrm{M}_n}+\mathrm{D}_i^T\frac{\nabla\mathrm{T}}{\mathrm{T}}\right)$ $\mathrm{D}_i^m=(1-\omega_i)\left(\sum_{k\neq1}\frac{\mathrm{x}_k}{\mathrm{D}_{ik}}\right)^{-1}$, $\mathrm{M}_n=\left(\sum_i\frac{\omega_i}{\mathrm{M}_i}\right)^{-1}$ (Mixture-averaged diffusion model)	Mass balance for the catalytic bed
Heat transfer in fluids	$\rho\mathrm{C}_P\cdot\nabla\mathrm{T}=\nabla\cdot(\kappa\nabla\mathrm{T})+\mathrm{Q}$	Energy balance for the catalytic bed
Heat transfer in solids	$0=\nabla\cdot(\kappa\nabla\mathrm{T})+\mathrm{Q}$ (with heat transfer by radiation being negligible)	Energy balance for the reactor body
Free and porous media flow	$\frac{\rho}{\varepsilon_P}\left((\mathbf{u}\cdot\nabla)\frac{\mathbf{u}}{\varepsilon_P}\right)=\mathbf{F}-\left(\frac{\mu}{\kappa_{br}}+\mathrm{Q}_{br}\right)\mathbf{u}$ $+\nabla\cdot\left[-\mathrm{P}\mathbf{I}+\frac{\mu}{\varepsilon_P}(\nabla\mathbf{u}+\nabla\mathbf{u}^T)-\frac{2\mu}{3\varepsilon_P}(\nabla\cdot\mathbf{u})\mathbf{I}\right]$ (Brinkman equation is for the porous media region, while the "Laminar flow" equation is used for the free media region)	Momentum balance for the catalytic bed

Multiphysics 6.1 (COMSOL, Inc.) and the balance equations were applied to each domain (the details are listed in Table 1) using built-in calculation modules in COMSOL Multiphysics.

RESULTS AND DISCUSSION

The kinetic rate equations developed in our previous work (lab-scale) [16] were used in CFD modeling because the same catalyst was used in the experiments.

$$\mathrm{R}_{C_1}=\frac{\mathrm{k}_{C_1}\mathrm{P}_{CO}\mathrm{P}_{H_2}}{(1+\mathrm{K}_{CO}\mathrm{P}_{CO}+\mathrm{K}_{H_2}\mathrm{P}_{H_2})^2} \quad (1)$$

$$\mathrm{R}_{C_{2\text{-}4}}=\frac{\mathrm{k}_{C_{2\text{-}4}}\mathrm{P}_{CO}\mathrm{P}_{H_2}}{(1+\mathrm{K}_{CO}\mathrm{P}_{CO}+\mathrm{K}_{H_2}\mathrm{P}_{H_2})^2} \quad (2)$$

$$\mathrm{R}_{C_{5+}}=\frac{\mathrm{k}_{C_{5+}}\mathrm{P}_{CO}\mathrm{P}_{H_2}}{(1+\mathrm{K}_{CO}\mathrm{P}_{CO}+\mathrm{K}_{H_2}\mathrm{P}_{H_2})^2} \quad (3)$$

where

$$\mathrm{k}_{C_1}=2.78\times10^{-5}\exp\left[-\frac{121{,}000}{\mathrm{R}}\left(\frac{1}{\mathrm{T}}-\frac{1}{503.15}\right)\right]$$

$$\mathrm{k}_{C_{2\text{-}4}}=1.17\times10^{-5}\exp\left[-\frac{163{,}000}{\mathrm{R}}\left(\frac{1}{\mathrm{T}}-\frac{1}{503.15}\right)\right]$$

$$\mathrm{k}_{C_{5+}}=3.69\times10^{-5}\exp\left[-\frac{64{,}000}{\mathrm{R}}\left(\frac{1}{\mathrm{T}}-\frac{1}{503.15}\right)\right]$$

$$\mathrm{K}_{H_2}=1.91\times10^{-4}\exp\left[-\frac{24{,}600}{\mathrm{R}}\left(\frac{1}{\mathrm{T}}-\frac{1}{503.15}\right)\right]$$

$$\mathrm{K}_{CO}=8.73\times10^{-2}\exp\left[-\frac{19{,}300}{\mathrm{R}}\left(\frac{1}{\mathrm{T}}-\frac{1}{503.15}\right)\right]$$

The units of k_i, K_{H_2}, and K_{CO} are mol/(kg_{cat}·s·bar^2), bar^{-1}, and bar^{-1}, respectively, and the gas constant (R) is 8.314 J/(mol·K).

A schematic of the pilot-scale reactor is presented in Figure 1b. The capacity of the reactor was 0.2 BPD. Although the inlet and outlet of the coolant channel were located at the side of the reactor (Fig. 1(a)), the counter-current flow for the reactant and coolant was assumed for simplicity. As shown in our previous study [16], the assumption resulted in slight differences in the simulation results (actual vs counter-current) because the width of the reactor body was insignificantly large. The symmetry condition was applied in the simulation to reduce the computational load.

Fig. 2 presents the conversion and temperature profiles along the reactor axis and cross-sectional view at the location of the maximum temperature (62 mm from the catalytic bed inlet), when the feed/coolant temperature, pressure, and space velocity were 225 °C, 20 bar, and 6,600 mL/(g_{cat}·h), respectively. The experimental and simulation data for conversion and selectivity are presented in Table 2, and their comparison, based on the absolute relative residuals defined as $M=100\times|(y_{i,sim}-y_{i,exp})/y_{i,exp}|$, shows that the model satisfactorily describes the pilot-scale FTS reactor with microscale cooling channels. This result validates the effectiveness of the developed model.

Fig. 2 shows that the conversion gradually increased along the reactor axis, whereas the temperature profile showed the peak temperature (241 °C) in the early part of the catalytic bed. This resulted in a temperature increase of 16 °C. The temperature was efficiently controlled by the microscale cooling channels, as observed in the almost isothermal operation at the later part of the catalytic bed, which accomplished 80% conversion. The thermal increase in the center of each catalytic bed was more significant than that in the area close to the boundary, as shown in the cross-view of the catalytic bed at the location of the maximum temperature. This feature indicates that the size of a single catalytic bed should be limited for efficient thermal control.

The size of each catalytic layer needs to be increased by increasing the number of single catalytic beds to increase the capacity of the reactor module. In such a case, the width of the reactor mod-

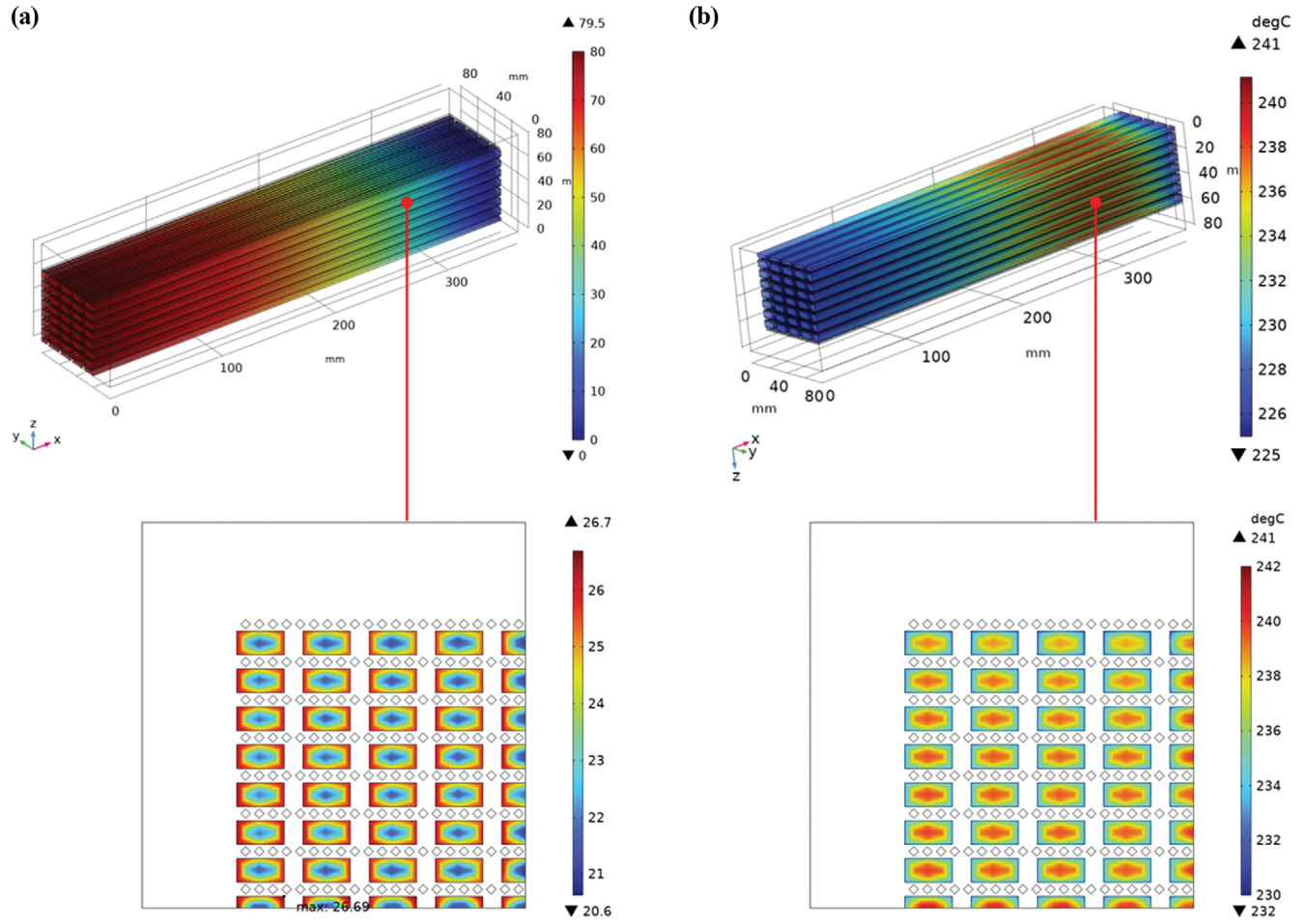


Fig. 2. (a) Temperature and (b) conversion profiles of the pilot-scale multichannel FTS reactor with microscale cooling channels. The figures in the box represent the cross-sectional view at 62 mm from the catalytic bed inlet (maximum temperature). The feed/coolant temperature, pressure, and space velocity are 225 °C, 20 bar, and 6,600 mL/(g_{cat}·h), respectively.

Table 2. Values of conversion and selectivity

		Experimental data	Simulation results	Relative error [%]†
Conversion [%]		74	79	6.73
Selectivity	CH_4	10	8.3	16.9
	C_2H_6-C_4H_{10}§	8.7	11	30.8
	C_{5+}§	81.3	80.3	1.22

§In the simulation, C_2H_6-C_4H_{10} and C_{5+} were represented by C_3H_8 and C_8H_{18}, respectively.

†The absolute relative errors were defined as $M=100\times|(y_{i,sim}-y_{i,exp})/y_{i,exp}|$, where the subscripts sim and exp denote the experimental data and simulation results, respectively.

ule becomes substantially large (Fig. 3(a)), and therefore, the coolant should be fed and discharged at the side of the module. However, thermal control may have been limited at the location where the cooling channel was not densely installed when coolant feeding was conducted on one side of the module. For example, considering that the peak temperature mostly appears in the early part of the packed-bed channel, the area near the red star in Fig. 3(b) may have lower heat transfer rates than the near coolant entrance caused by the low density of the cooling channels. Two symmetric-structured microscale cooling channel layers were considered and installed alternately between the catalytic layers to prevent the biased temperature increase.

CFD modeling was conducted for the mirrored and nonmirrored (only one type of microscale cooling channel was used) cases to compare the performance of thermal control. The upper half of the module is simulated because of the symmetry of the reactor module, and the results are illustrated in Fig. 4. For comparison, the temperature scale is fixed to the same value between cases. The

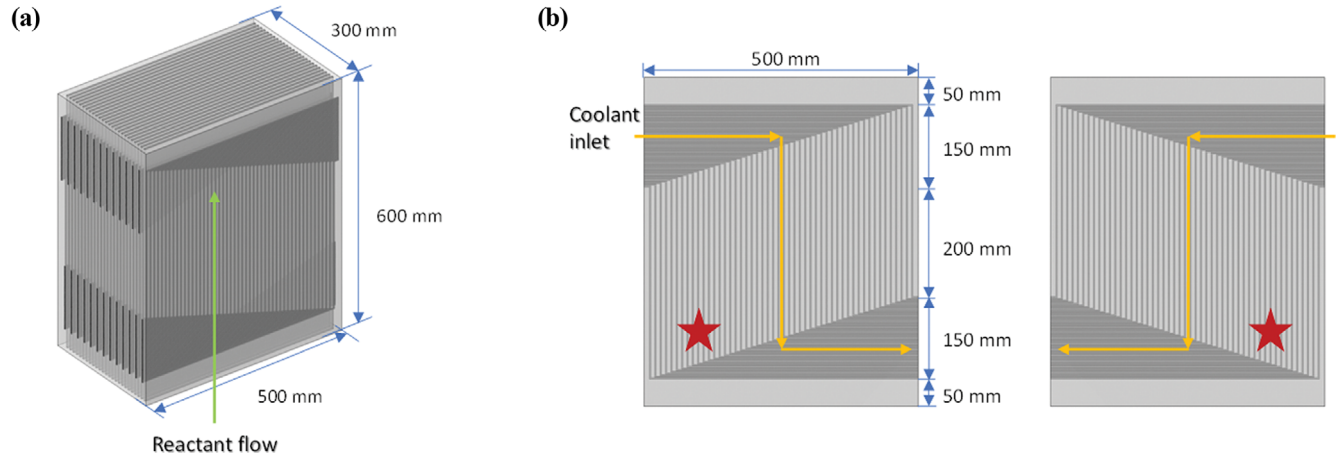


Fig. 3. Schematic of (a) the multichannel FTS reactor with microscale cooling channels suggested in the present study. The number of the catalytic-bed layers is 25 and (b) two symmetric-structured microscale cooling channel layers, alternately stacked between the catalytic-bed layers (the number of each structure is 13, and the total number of cooling layers is 26). The red star represents the area with a low density of microscale cooling channels.

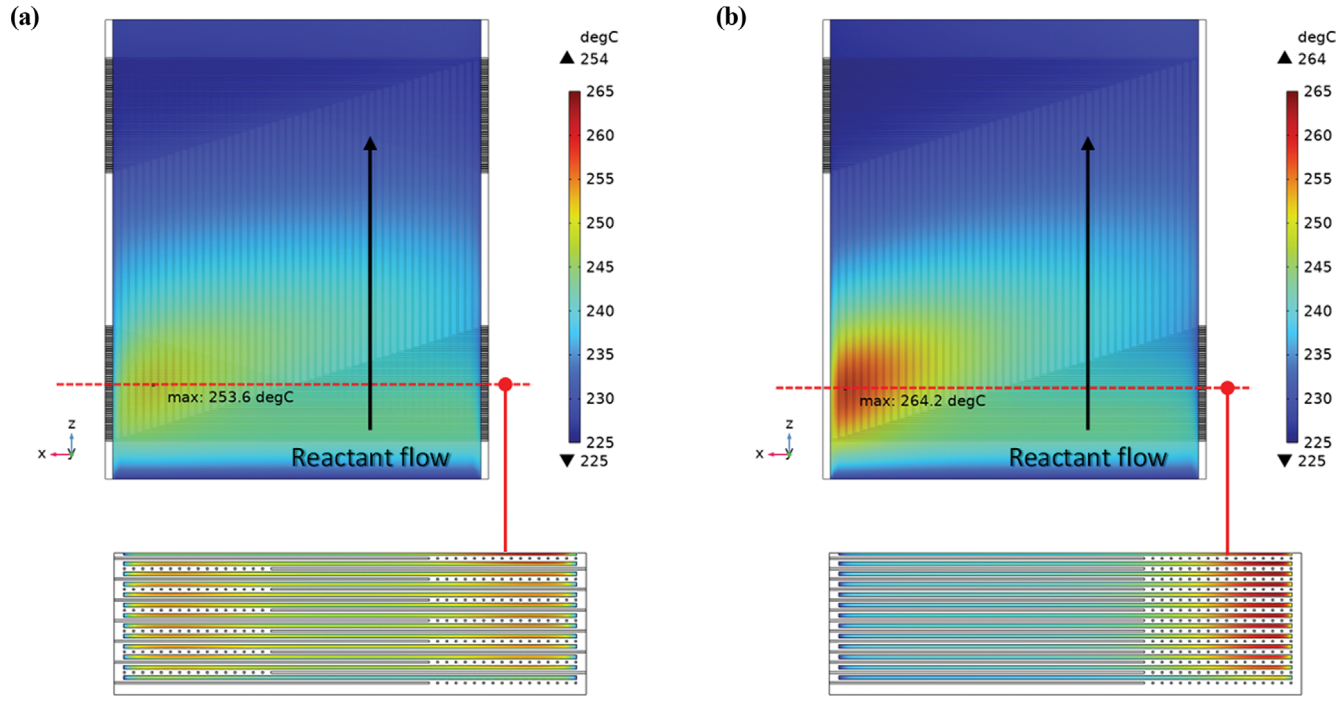


Fig. 4. Temperature profiles of the center catalytic layer (13th) when (a) two symmetric-structured cooling layers were used (mirrored structure) and (b) one type of cooling layer (the left one in Fig. 3(b)) was used (nonmirrored structure). Cross-sectional view images of the reactor (lower half) at the location of the maximum temperature are provided below each figure. The maximum temperatures for the mirrored and nonmirrored structures are 253.6 and 264.2 °C, respectively. The feed/coolant temperature, pressure, and space velocity are 225 °C, 20 bar, and 6,600 mL/(g_{cat}·h), respectively.

thermal increase in the mirror-structured module (ΔT_{max}=28.6 °C, Fig. 4(a)) is lower than that of the nonmirrored module (ΔT_{max}= 39.2 °C, Fig. 4(b)). Further, as shown in the cross-sectional view of the module at the location of the maximum temperature, the mirrored structure resulted in a more even distribution of temperature than the nonmirrored structure, which indicates that a more stable operation can be achieved by using the mirrored structure. Table 3 summarizes that a high peak temperature in the nonmirrored structure led to a slightly higher conversion than that of the mirrored structure, whereas an even temperature distribution in the mirrored structure resulted in higher C_{5+} selectivity than that of the nonmirrored case. An approximately 1% increase in the yield of C_{5+} (desired product) is meaningful, especially in the industrial production.

Table 3. Values of conversion and selectivity between the mirrored and nonmirrored structures

		Mirrored	Nonmirrored
Conversion [%]		84.57	84.97
Selectivity	CH_4	9.31	9.51
	C_2H_6-C_4H_{10} [$]	14.43	15.27
	C_{5+} [$]	76.25	75.22

[$]In the simulation, C_2H_6-C_4H_{10} and C_{5+} were represented by C_3H_8 and C_8H_{18}, respectively.

Fig. 5 shows the effects of the feed/coolant temperature on the temperature profile of the center catalytic layer. The maximum temperature increased exponentially with an increase in the operating temperature; the location of the hot spot became closer to the inlet of the catalytic bed and a gradual increase in low temperature turned into a steep increase at high temperature, which indicates that the reaction significantly occurred in the early part of the reactor at high temperatures. Fig. 5 shows that the location of the hot spot changes alternately between the left and right sides of the catalytic layer because of the alternating installation of the mirrored structure.

The increase in space velocity showed that the location of the maximum temperature moved in the direction of the outlet (Fig. 6) because high linear velocity increased heat convection, whereas the degree of temperature increase was not as significant as that in the case of the feed temperature change. Although high space velocity decreased conversion, the increased amount of feed corresponded to high heat generation (proportional to the multiplication of conversion and feed flow rate). Therefore, it is shown that the module can be stably operated even at high space velocity.

The effects of pressure on thermal behavior in the catalytic bed were similar to those of temperature change (Fig. 7). The peak temperature was proportional to pressure, whereas the corresponding location was inversely proportional. This feature is attributable to the high concentration of the reactant at high pressure, which resulted in a high reaction rate (steep temperature increase).

The effects of operating conditions on conversion, C_{5+} selectivity, and peak temperature were further investigated. Fig. 8(a) shows the proportional relationship between the conversion and the tem-

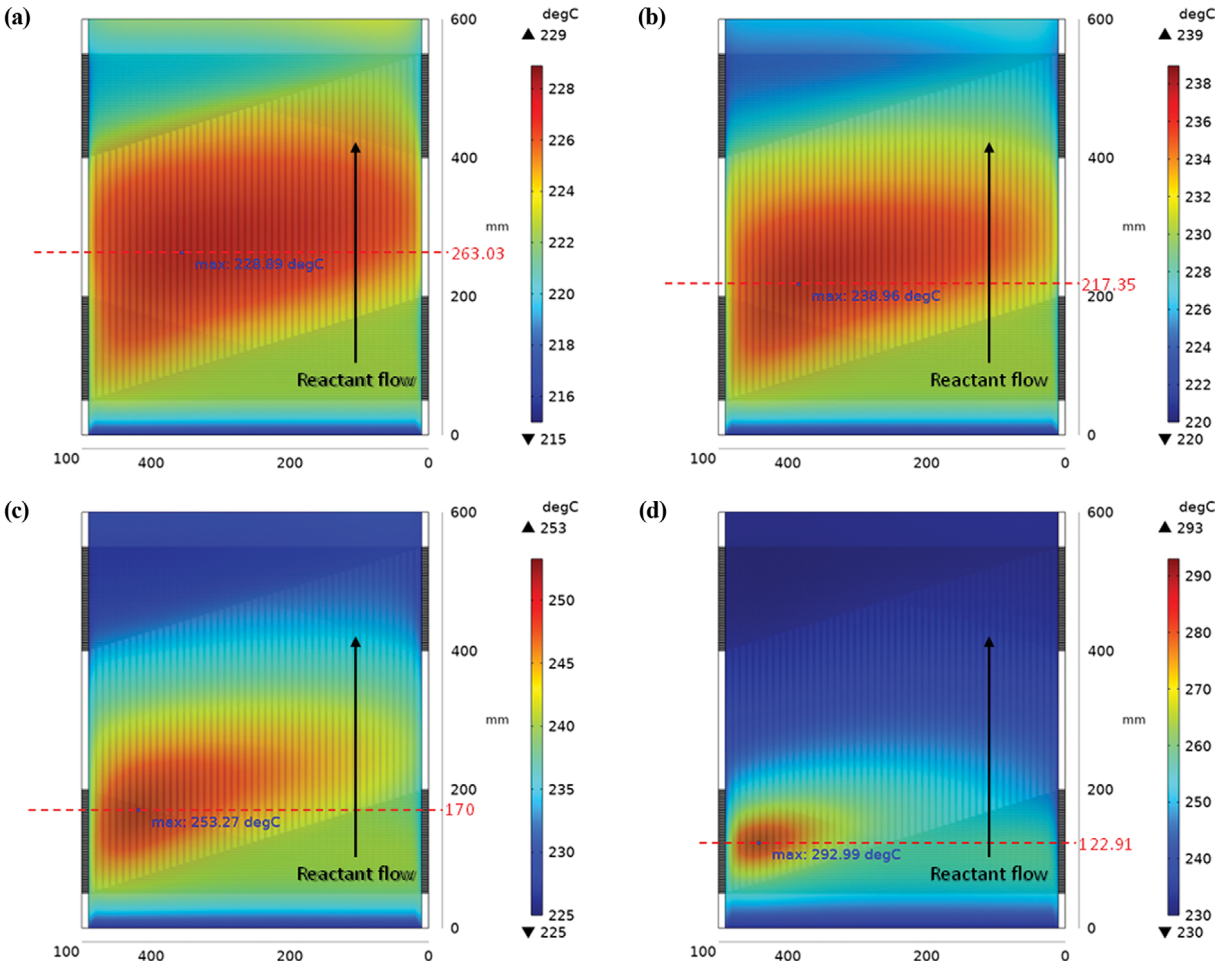


Fig. 5. Temperature profiles of the center catalytic layer (13th) at feed/coolant temperatures of (a) 215 °C, (b) 220 °C, (c) 225 °C, and (d) 230 °C. The pressure and space velocity are 20 bar and 8,000 mL/(g_{cat}·h), respectively. The red-dotted line represents the location of the maximum temperature (values in blue vs. location in red-colored numbers), and the maximum temperatures are 228.89, 238.96, 253.27, and 292.99 °C for diagrams (a)-(d), respectively.

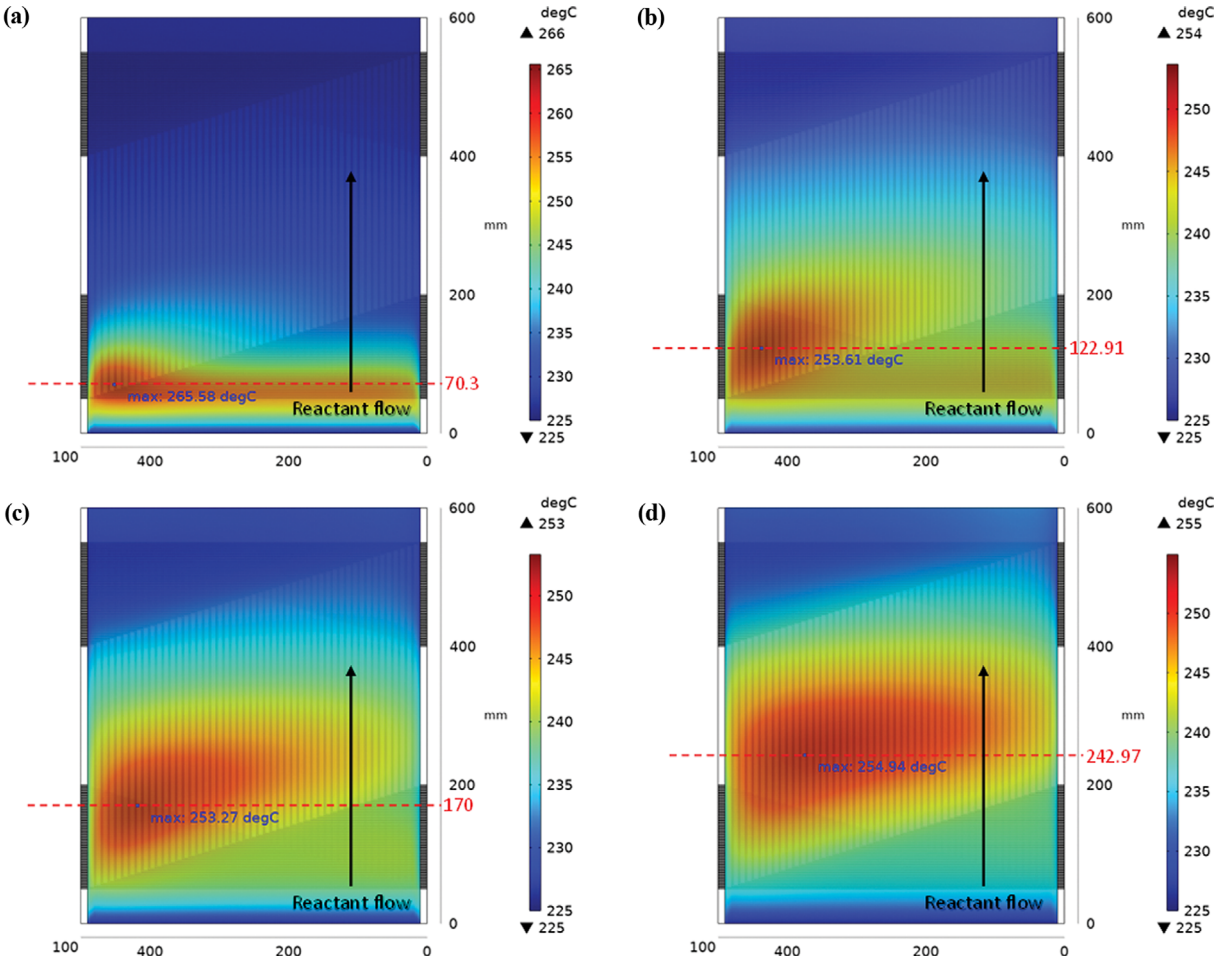


Fig. 6. Temperature profiles of the center catalytic layer (13th) at space velocities of (a) 5,000 mL/(g_{cat}·h), (b) 6,600 mL/(g_{cat}·h), (c) 8,000 mL/(g_{cat}·h), and (d) 10,000 mL/(g_{cat}·h). The feed/coolant temperature and pressure are 225 °C and 20 bar, respectively. The red-dotted line represents the location of the maximum temperature (values in blue vs. location in red numbers), and the maximum temperatures are 265.58, 253.61, 253.27, and 254.94 °C for diagrams (a)-(d), respectively.

perature, whereas the positive effects of space velocity are observed at low temperature. Therefore, high conversion was achieved at high temperature irrespective of the space velocity. The effects of space velocity on C_{5+} selectivity are negligible (Fig. 8(b)), whereas the negative effects of temperature are clearly shown, which is a well-known property of the Fischer-Tropsch synthesis that high temperature produces short chains. This feature indicates a trade-off of temperature between the conversion and C_{5+} selectivity; there might be an optimal temperature for the maximum C_{5+} yield. Figs. 5 and 6 show the insignificant influence of space velocity and the exponential relationship between the temperature and the degree of hot spot (Fig. 8(c)). Detailed values of CFD modeling results under a variety of space velocities and temperatures and the fitting results are provided in the Supplementary Information.

The positive effects of both temperature and pressure on conversion and the maximum temperature were observed, and the negative effects on C_{5+} selectivity are illustrated (Figs. 8(d) to 8(f)). Based on the analysis, a trade-off of the C_{5+} yield between the temperature and pressure can be inferred. Therefore, the optimal conditions for temperature, space velocity, and pressure should be determined using the CFD modeling-based strategy after the design of the industrial reactor module was completed.

CONCLUSIONS

A CFD simulation successively described the detailed distributions of conversion and temperature of both the catalytic and cooling layers of the multichannel Fischer-Tropsch reactor with microscale cooling channels. After the validity of the developed model was corroborated by the comparison between the experimental data from the pilot plant and simulation results, the model was extended to the novel structure of the reactor, wherein the mirrored structure cooling layers suggested in the present study were alternately stacked to obviate local hot spots. The simulation showed that the symmetric distribution of the dense cooling channel area in the early part of the reactor decreased peak temperatures, whereas the nonmirrored case resulted in hot spots because of the limited heat transfer capacity. Further analysis of the effects of operating conditions on the catalytic performance and thermal stability of the proposed structure showed trade-offs between the operating variables.

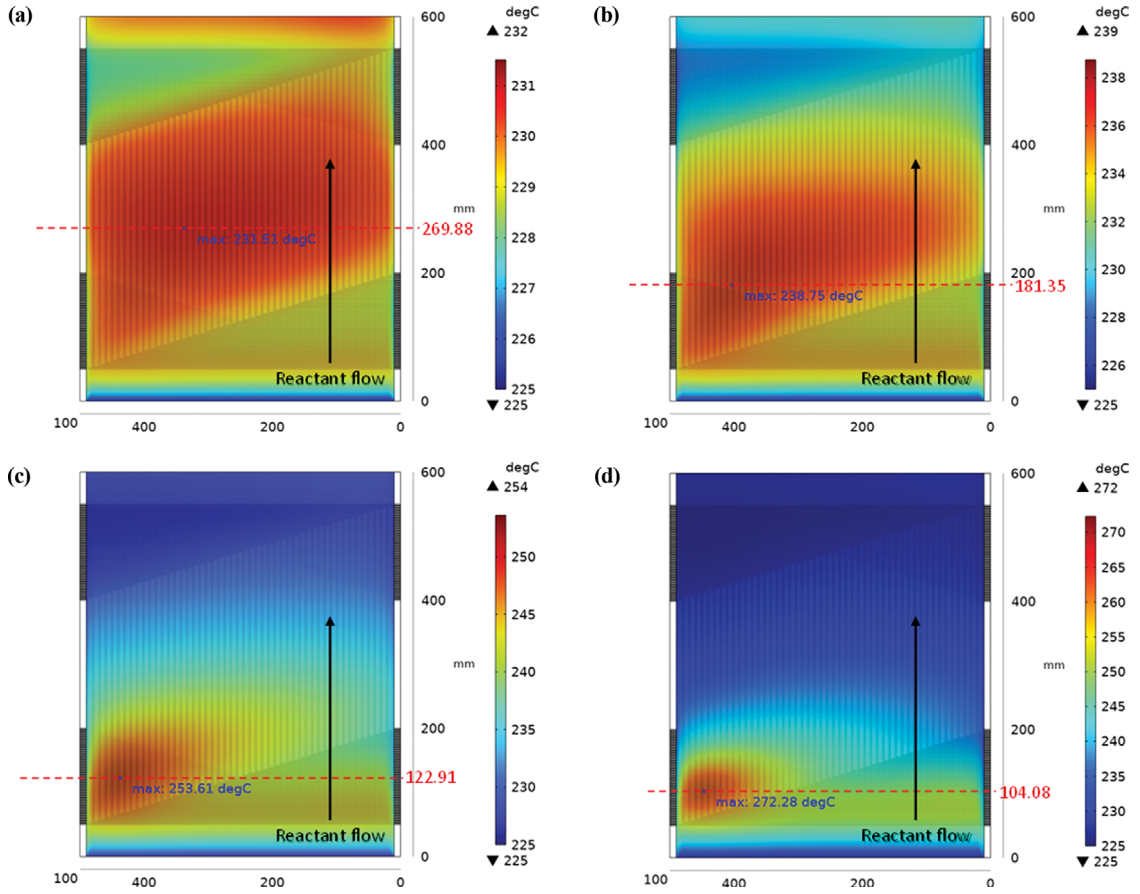


Fig. 7. Temperature profiles of the center catalytic layer (13th) at pressures of (a) 10 bar, (b) 15 bar, (c) 20 bar, and (d) 22 bar. The feed/coolant temperature and space velocity are 225 °C and 6,600 mL/(g_{cat}·h), respectively. The red-dotted line represents the location of the maximum temperature (values in blue vs. location in red-colored numbers), and the maximum temperatures are 231.51, 238.75, 253.61, and 272.28 °C for diagrams (a)-(d), respectively.

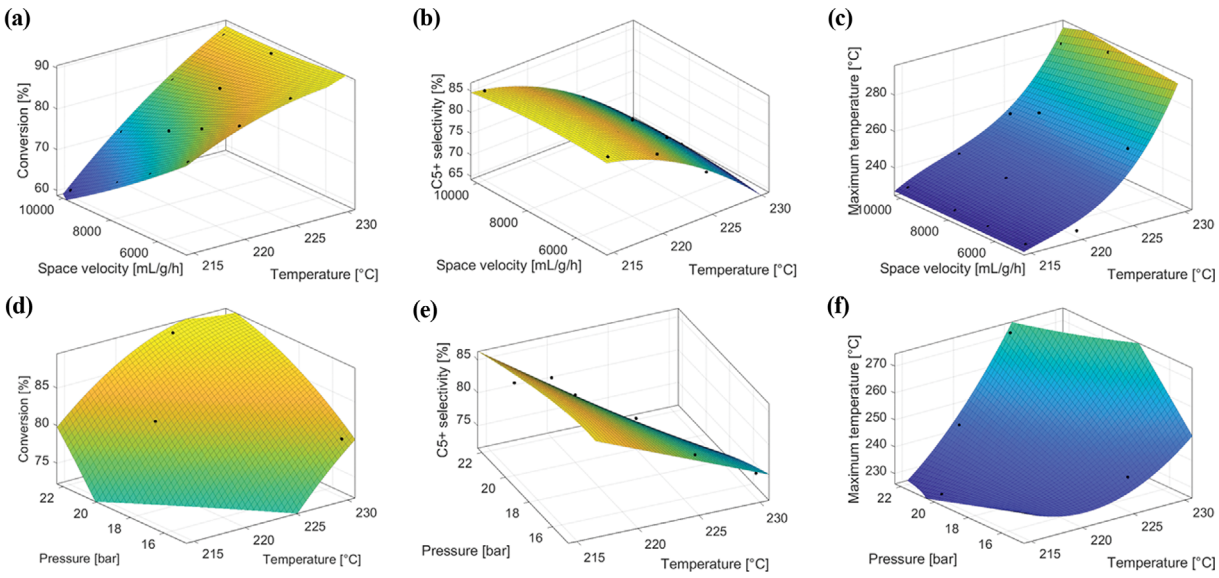


Fig. 8. Effects of feed/coolant temperature and space velocity on (a) conversion [%], (b) C_{5+} selectivity [%], and (c) maximum temperature [°C] at the pressure of 20 bar. The effects of feed/coolant temperature and pressure on (d) conversion [%], (e) C_{5+} selectivity [%], and (f) maximum temperature [°C] at the space velocity of 6,600 mL/(g_{cat}·h). Black dots correspond to CFD modeling (Table S1 in the Supplementary Information) and the surface represents the regressed curve (the fitting results are provided in Table S2 in the Supplementary Information).

In conclusion, the application of the CFD model is an efficient way to understand the detailed dynamics of the and to design a novel structure for enhanced thermal capacity multichannel Fischer-Tropsch reactor with microscale cooling channels.

ACKNOWLEDGEMENTS

This research was supported by the Research Project for "Carbon Upcycling Project for Platform Chemicals" of the National Research Foundation (NRF) funded by the Ministry of Science and ICT (Grant number: 2022M3J3A104602111).

NOMENCLATURE

C_P : heat capacity [J/(kg·K]
D_i^m : mixture-averaged diffusion coefficient of species i [m^2/s]
D_i^T : thermal diffusion coefficient of species i [kg/(m·s)]
D_{ik} : multicomponent Maxwell-Stefan diffusivities of species i and k [m^2/s]
F : volume force [N/m^3]
I : identity matrix
$\mathbf{j}_i$: mass flux of species i [kg/(m^2·s)]
M_n : mean molar mass [kg/mol]
Q : heat source term [W/m^3]
Q_{br} : mass source term [kg/(m^3·s)]
u : velocity vector [m/s]
ω_i : mass fraction of species i [dimensionless]

Greek Letters

ε_P : porosity [dimensionless]
κ : thermal conductivity [W/(m·K)]
κ_{br} : permeability of the porous medium [m^2]
μ : dynamic viscosity [Pa·s]
ρ : fluid density [kg/m^3]

SUPPORTING INFORMATION

Additional information as noted in the text. This information is available via the Internet at http://www.springer.com/chemistry/journal/11814.

REFERENCES

1. M. E. Dry, *Catal. Today*, **71**, 227 (2002).
2. C. Song, *Catal. Today*, **115**, 2 (2006).
3. T. K. Das, W. A. Conner, J. Li, G. Jacobs, M. E. Dry and B. H. Davis, *Energy Fuels*, **19**, 1430 (2005).
4. W. Ma, G. Jacobs, D. E. Sparks, R. L. Spicer, B. H. Davis, J. L. S. Klettlinger and C. H. Yen, *Catal. Today*, **228**, 158 (2014).
5. R. Zennaro, M. Tagliabue and C. H. Bartholomew, *Catal. Today*, **58**, 309 (2000).
6. I. C. Yates and C. N. Satterfield, *Energy Fuels*, **5**, 168 (1991).
7. K. Keyvanloo, S. J. Lanham and W. C. Hecker, *Catal. Today*, **270**, 9 (2016).
8. Y. Sun, G. Yang, L. Zhang and Z. Sun, *Chem. Eng. Process.*, **119**, 44 (2017).
9. N. Moazami, M. L. Wyszynski, K. Rahbar, A. Tsolakis and H. Mahmoudi, *Chem. Eng. Sci.*, **171**, 32 (2017).
10. M. Ostadi, E. Rytter and M. Hillestad, *Chem. Eng. Res. Des.*, **114**, 236 (2016).
11. L. Fratalocchi, C. G. Visconti, G. Groppi, L. Lietti and E. Tronconi, *Chem. Eng. J.*, **349**, 829 (2018).
12. S. R. Deshmukh, A. L. Y. Tonkovich, K. T. Jarosch, L. Schrader, S. P. Fitzgerald, D. R. Kilanowski, J. J. Lerou and T. J. Mazanec, *Ind. Eng. Chem. Res.*, **49**, 10883 (2010).
13. D.-Y. Shin, K.-S. Ha, M.-J. Park, G. Kwak, Y.-J. Lee and K.-W. Jun, *Fuel*, **158**, 826 (2015).
14. G. Arzamendi, P. M. Diéguez, M. Montes, J. A. Odriozola, E. Falabella Sousa-Aguiar and L. M. Gandía, *Chem. Eng. J.*, **160**, 915 (2010).
15. M.-S. Shin, N. Park, M.-J. Park, J.-Y. Cheon, J. K. Kang, K.-W. Jun and K.-S. Ha, *Fuel Process. Technol.*, **118**, 235 (2014).
16. J.-S. Park, D.-E. Kim, Y.-J. Lee, G. Kwak, K.-W. Jun and M.-J. Park, *Ind. Eng. Chem. Res.*, **55**, 9416 (2016).
17. K. S. Kshetrimayum, I. Jung, J. Na, S. Park, Y. Lee, S. Park, C.-J. Lee and C. Han, *Ind. Eng. Chem. Res.*, **55**, 543 (2016).
18. S. Saeidi, M. K. Nikoo, A. Mirvakili, S. Bahrani, N. A. S. Amin and M. R. Rahimpour, *Rev. Chem. Eng.*, **31**, 209 (2015).

Supporting Information

CFD modeling of a multichannel Fischer-Tropsch reactor module with microscale cooling channels: Effects of mirrored structure cooling layers

Yesol Woo*, Da Bin Oh, Jae Eun Park**, Seung Ju Han***, Yun-Jo Lee***, and Myung-June Park*,**,†**

*Department of Energy Systems Research, Ajou University, Suwon 16499, Korea
**Department of Chemical Engineering, Ajou University, Suwon 16499, Korea
***C1 Gas & Carbon Convergent Research Center, Korea Research Institute of Chemical Technology (KRICT), Daejeon 34114, Korea
(*Received 28 March 2023 • Revised 15 May 2023 • Accepted 22 May 2023*)

Table S1. CFD simulation results for the FTS reactor with the mirror-structured cooling microchannels presented in this study

	Feed/coolant temperature [°C]	Space velocity [mL/g_{cat}/h]	Conversion [%]	C_{5+} selectivity [%]	Maximum temperature [°C]	Remarks
1	215	5,000	80.35	85.88	228.01	
2	215	6,600	73.1	85.62	228.29	
3	215	8,000	67.33	85.42	228.89	
4	215	10,000	60.18	85.22	229.50	
5	220	5,000	85.83	82.00	228.01	
6	220	6,600	80.87	81.78	238.30	Effects of temperature and space velocity
7	220	8,000	76.67	81.39	238.96	
8	220	10,000	71.10	80.84	240.22	
9	225	5,000	89.14	73.32	265.58	
10	225	6,600	84.57	76.25	253.61	
11	225	8,000	83.69	75.87	253.27	
12	225	10,000	80.44	74.71	254.94	
13	230	8,000	88.87	65.63	292.99	
14	230	10,000	87.97	65.24	285.81	
	Feed/coolant temperature [°C]	Pressure [bar]	Conversion [%]	C_{5+} selectivity [%]	Maximum temperature [°C]	Remarks
15	215	20	73.1	85.62	228.29	
16	220	20	80.87	81.78	238.35	
17	220	22	84.83	80.65	243.16	Effects of temperature and pressure
18	225	15	73.03	80.14	238.75	
19	225	20	84.57	76.25	253.6	
20	225	22	88.74	72.21	272.28	
21	230	15	80.00	75.33	249.08	

Table S2. Fitting polynomials and the fitted values of the parameters for the effects of operating conditions

Independent variables	Output variable	Parameters (95% confidence interval)	R^2
Temperature (x) and space velocity (y)	Conversion=p00+p10*x+p01*y +p20*x^2+p11*x*y+p02*y^2	p00=−3617 (−1.092e+04, 3686), p10=27.12 (−33.61, 87.86), p01=54.89 (−20.38, 130.2), p20=−0.04979 (−0.1764, 0.07682), p11=−0.1974 (−0.5286, 0.1337), p02=−0.2228 (−0.37, −0.07553)	0.9978
	Selectivity=p00+p10*x+p01*y +p20*x^2+p11*x*y+p02*y^2	p00=−2497 (−3470, −1523), p10=24.65 (15.73, 33.56), p01=−0.004306 (−0.0164, 0.007787), p20=−0.0589 (−0.07937, −0.03842), p11=2.781e−05 (−2.779e−05, 8.341e−05), p02=−1.246e−07 (−2.81e−07, 3.177e−08)	0.9935
	T_{max}=p00+p10*x+p01*y+p20*x^2 +p11*x*y+p30*x^3+p21*x^2*y	p00=−1.917e+05 (−1.393e+06, 1.01e+06), p10=2698 (−1.364e+04, 1.904e+04), p01=−1.574 (−14.63, 11.48), p20=−12.64 (−86.78, 61.5), p11=0.01441 (−0.1038, 0.1327), p30=0.01975 (−0.09245, 0.1319), p21= −3.297e−05 (−0.0003006, 0.0002347)	0.7968
Temperature (x) and pressure (y)	Conversion=p00+p10*x+p01*y +p20*x^2+p11*x*y+p02*y^2	p00=−3006 (−2.288e+04, 1.687e+04), p10=22.86 (−140.2, 185.9), p01=41.5 (−195.3, 278.3), p20=−0.04207 (−0.379, 0.2948), p11=−0.1577 (−1.103, 0.7878), p02=−0.1034 (−1.362, 1.155)	0.9956
	Selectivity=p00+p10*x+p01*y +p11*x*y+p02*y^2	p00=33.16 (−1658, 1724), p10=0.1852 (−6.914, 7.284), p01=15.6 (−75.89, 107.1), p11=−0.06418 (−0.4261, 0.2977), p02=−0.0557 (−0.6968, 0.5854)	0.9603
	T_{max}=p00+p10*x+p01*y +p20*x^2+p11*x*y	p00=9952 (−2.292e+04, 4.283e+04), p10=−79.7 (−354.1, 194.7), p01=−130.2 (−476.2, 215.8), p20=0.161 (−0.412, 0.734), p11=0.5986 (−0.9426, 2.14)	0.9545